# Molecular Dynamics Studies of Dislocations in CdTe Crystals from a New Bond Order Potential

Xiaowang Zhou,*,[†] Donald K. Ward,[‡] Bryan M. Wong,[§] F. Patrick Doty,[‡] and Jonathan A. Zimmerman[†]

[†]Mechanics of Materials Department, [‡]Radiation and Nuclear Detection Materials and Analysis Department, and [§]Materials Chemistry Department, Sandia National Laboratories, Livermore, California 94551, United States

ABSTRACT: $Cd_{1-x}Zn_xTe$ (CZT) crystals are the leading semiconductors for radiation detection, but their application is limited by the high cost of detector-grade materials. High crystal costs primarily result from property nonuniformity that causes low manufacturing yield. Although tremendous efforts have been made in the past to reduce Te inclusions/precipitates in CZT, this has not resulted in an anticipated improvement in material property uniformity. Moreover, it is recognized that in addition to Te particles, dislocation cells can also cause electric field perturbations and the associated property nonuniformities. Further improvement of the material, therefore, requires that dislocations in CZT crystals be understood and controlled. Here, we use a recently developed CZT bond order potential to

perform representative molecular dynamics simulations to study configurations, energies, and mobilities of 29 different types of possible dislocations in CdTe (i.e., $x = 1$) crystals. An efficient method to derive activation free energies and activation volumes of thermally activated dislocation motion will be explored. Our focus gives insight into understanding important dislocations in the material and gives guidance toward experimental efforts for improving dislocation network structures in CZT crystals.
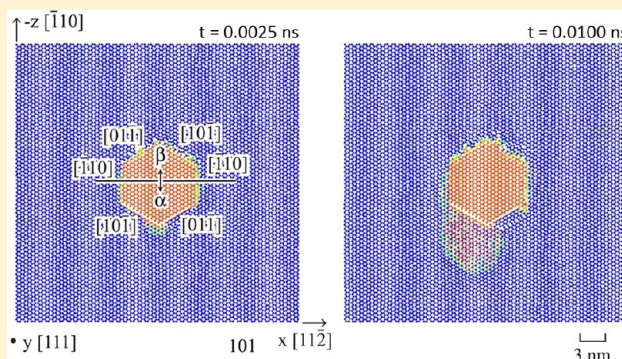
I. INTRODUCTION

Although CdTe-based CZT ($Cd_{1-x}Zn_xTe$) crystals are the leading semiconductor compounds for radiation-detection applications,[1−4] the widespread deployment of CZT detectors has been limited by the high cost (due to a low manufacturing yield) of detector-grade materials. Property nonuniformity has been the major cause for both poor performance and a low yield of usable portions of ingots.[1] It has long been established that micrometer-scale defects such as tellurium inclusions/precipitates affect carrier transport and uniformity.[1,5,6] However, extensive previous efforts to reduce Te particles have not resulted in an anticipated improvement in CZT property uniformity. One special structural feature of CZT crystals is their extreme softness and their propensity to always develop a high density of dislocations during synthesis.[7−9] Experiments have shown that when these dislocations are organized into a network of subgrains, they can directly affect charge carriers[10,11] to cause electric field perturbations. The subgrain boundaries can also serve as nucleation sites for tellurium precipitates.[1] Clearly, eliminating or at least controlling dislocation subgrain structures holds great potential to further improve CZT crystals.

Many types of dislocations may be present in CZT crystals, including shuffle dislocations, glide dislocations, α and β dislocations, partial and perfect dislocations, edge, screw, mixed dislocations, and misfit dislocations. The understanding of the behavior of the various combinations of these dislocations in conjunction with developing methods for improving the corresponding dislocation network structures are therefore

challenging. The use of predictive, high-fidelity atomistic simulations can help screen out these structure-limiting dislocation types. Here we use a recently developed CZT bond order potential (BOP)[12−14] in LAMMPS (large-scale atomic/molecular massively parallel simulator)[15,16] to perform selected molecular dynamic (MD) simulations to determine configurations, energies, and mobilities of 29 different types of dislocations in CdTe crystals. [The CZT ternary BOP[14] is an extension of the CdTe binary BOP,[12] so they are equivalent if used only for CdTe.] An efficient method to derive activation free energy and activation volume of thermally activated dislocation motion will be explored. Our focus is to identify and validate important dislocations and dislocation phenomena in the material, which can reduce future experimental efforts to improve the dislocation network structures.

II. INTERATOMIC POTENTIAL

The key to high-fidelity MD simulations of dislocations is an interatomic potential that is transferrable to the dislocated regions where the local atomic environment is significantly different from that of the perfect bulk crystal. Details of the CZT bond order potential applied here are omitted as they are very complex and have been fully described previously.[12−14] It is demonstrated that the CZT BOP captures well the property

trends of a variety of elemental and compound structures/ phases (with local environment varying from coordination 2 to 12),[12−14] simulates correctly the crystalline growth of stoichiometric compounds during both vapor deposition (under nonstoichiometric vapor fluxes)[17] and melt-growth[18] processes, and predicts precisely the configuration and density of misfit dislocations in vapor deposited multilayers.[19] Note that the correct simulation of growth, especially under a nonstoichiometric environment, is a very strong validation of the transferability of a potential as the process involves chemical reactions and samples a variety of configurations and chemistries statistically formed on a growth surface. For this reason, the CZT BOP is expected to produce reasonable results regarding dislocations.

III. DEFINITION OF DISLOCATION TYPES

Different types of dislocations can be constructed on various planes in a zinc-blende crystal. For instance, mobile dislocations usually lie on the {111} slip planes, and misfit dislocations in multilayered films are often seen to lie on interfacial planes,[19] which are not necessarily parallel to {111}. Here we only study dislocations that are on the {111} slip planes, with Burgers vector $\vec{b}$ being either partial <112>a/6 or perfect <110>a/2.

Assuming that the dislocation line direction $\vec{\xi}$ aligns with the z direction and the slip occurs on the x−z plane, our definition of different types of dislocations is shown in Figures 1 and 2,
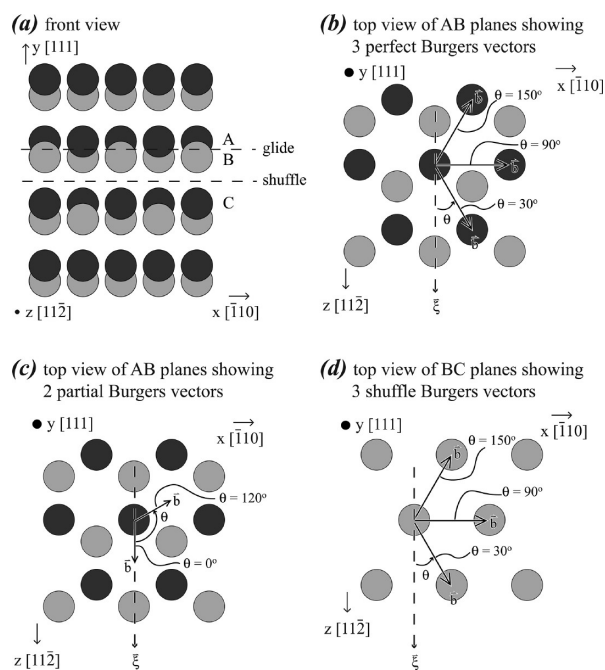
Figure 1. Geometry of the edge coordinate system. (a) Front projection of (11$\bar{2}$) planes, (b) top projection of two (111) planes A and B showing glide perfect dislocations, (c) top projection of two (111) planes A and B showing glide partial dislocations, and (d) top projection of two (111) planes B and C showing shuffle dislocations.

where dark and light circles distinguish metal (Cd or Zn) and Te atoms, respectively. Dislocations defined in Figure 1 are based upon an edge dislocation coordinate system shown in Figure 1a where the dislocation line $\vec{\xi}$ is perpendicular to one of the Burgers vectors <110>a/2 (x axis). Dislocations defined in Figure 2 are based upon a screw dislocation coordinate system shown in Figure 2a where $\vec{\xi}$ is parallel to one of the perfect
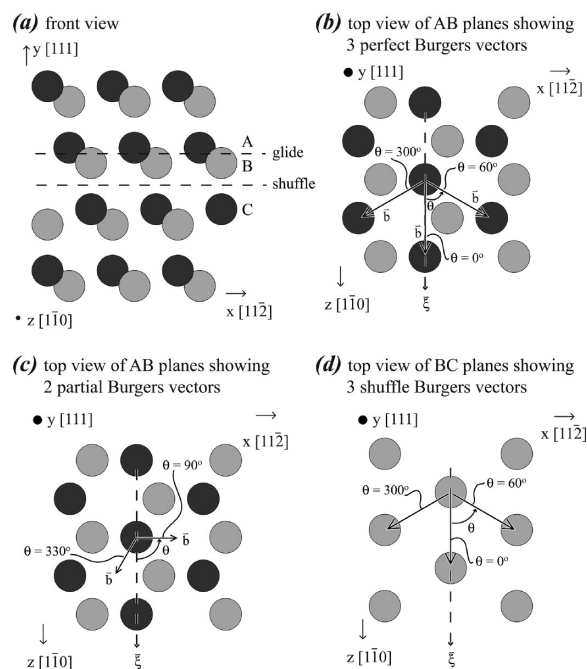
Figure 2. Geometry of the screw coordinate system. (a) front projection of (1$\bar{1}$0) planes, (b) top projection of two (111) planes A and B showing glide perfect dislocations, (c) top projection of two (111) planes A and B showing glide partial dislocations, and (d) top projection of two (111) planes B and C showing shuffle dislocations.

Burgers vectors <110>a/2 (z axis). Figures 1a and 2a indicate that a dislocation slip can occur at two different locations, one between two closely separated planes A and B (where the interplane bonds are not perpendicular to the planes), and the other between the more widely separated planes B and C (where the interplane bonds are perpendicular to the planes). According to convention, dislocations between A and B are called glide dislocations, and dislocations between planes B and C are called shuffle dislocations.

Burgers vectors of glide dislocations can be examined from a top projection of two isolated planes A and B. Figures 1b and 2b use such a projection to explore perfect dislocation Burgers vectors (<110>a/2). It can be seen from Figure 1b that in the edge coordinate system, there are three nonequivalent perfect Burgers vectors that can be represented by the angle θ between $\vec{b}$ and $\vec{\xi}$, i.e., θ = 30°, 90°, and 150°. There are other perfect Burgers vectors, but they are equivalent to the ones listed due to crystal symmetry. For instance, the θ = 330° dislocation is equivalent to the θ = 30° dislocation. Similarly, it can be seen from Figure 2b that in the screw coordinate system there are three more nonequivalent perfect Burgers vectors θ = 0°, 60°, and 300°.

Figures 1c and 2c use the same top projection of two isolated planes A and B to explore partial dislocation Burgers vectors (<112>a/6). It can be seen from Figure 1c that in the edge coordinate system, there are two nonequivalent partial Burgers vectors θ = 0° and 120°. Similarly, it can be seen from Figure 2c that in the screw coordinate system there are two more nonequivalent partial Burgers vectors θ = 90° and 330°.

Burgers vectors of shuffle dislocations can be examined from the top projection of two isolated planes B and C. Figures 1d and 2d use such a projection to explore shuffle dislocation Burgers vectors. Here the light and dark atoms in the B and C planes are aligned in the projection (i.e., only light atoms are

seen), and hence, there are no partial dislocation Burgers vectors for shuffle dislocations. As indicated in Figure 1d for the edge coordinate system, we explore three shuffle dislocation Burgers vectors $\theta = 30°$, $90°$, and $150°$, which are the same as those in the perfect glide dislocation case shown in Figure 1b. As indicated in Figure 2d for the screw coordinate system, we explore three more shuffle dislocation Burgers vectors $\theta = 0°$, $60°$, and $300°$, which are the same as those in the perfect glide dislocation case shown in Figure 2b.

Dislocations shown in Figures 1 and 2 always occur between a metal (Cd or Zn) and Te {111} planes. If a dislocation has an edge component, then the dislocation core can have extra metal atoms or extra Te atoms. According to convention, a dislocation with more metal atoms at its core is called an α dislocation, and a dislocation with more Te atoms at its core is called a β dislocation.

According to the discussion above, we will consider a combination of glide and shuffle dislocations, partial and perfect dislocations, various Burgers vectors, and α and β dislocations. These constitute 29 different types of dislocations as listed in Table 1.

IV. STACKING FAULT ENERGY

A CdTe crystal system with 336 $(11\bar{2})$ planes in the x direction, 60 (111) planes in the y direction, and 28 $(1\bar{1}0)$ planes in the z direction is used to calculate the (111) stacking fault energy γ_{sf}. The stacking fault is created by shifting the upper part of a perfect crystal by a partial dislocation vector with respect to the lower part (at a glide dislocation slip plane between planes A and B, see Figure 1 or 2). Molecular statics (MS) energy minimization simulations are used to calculate relaxed energies of both the perfect and the stacking faulted crystals under the periodic boundary conditions in both x and z directions and a free boundary condition in y direction. The stacking fault energy is then calculated as $\gamma_{sf} = (E_{sf} - E_0)/(L_x L_z)$, where E_{sf} and E_0 are respectively the relaxed energies for stacking faulted and perfect crystals and L_x and L_z are respectively the system dimensions in x and z directions. Note that the surface energy in the y direction does not affect the calculation as it exists for both stacking faulted and perfect crystals and therefore cancels out. We find that $\gamma_{sf} \approx 0$ in our calculations. In the literature, CdTe is known to have a low stacking fault energy around 10 mJ/m².[20,21]

V. DISLOCATION LINE ENERGIES

Linear elastic continuum theory cannot describe dislocation core structures. Atomistic simulations allow direct studies of dislocation core structures. This in turn allows dislocation energies, i.e., the energy difference between a dislocated crystal and a perfect CdTe crystal containing the same number of atoms, to be calculated as a function of dislocation core radius. The key for the calculations is to use the initial dislocation configurations that can be fully relaxed during MD and MS energy minimization simulations. Different methods have been tried to create initial dislocations. We find that an initial dislocation created by simply positioning atoms according to the displacement field of the linear elastic continuum solution does not always fully relax at the core. Instead, a dislocation created by shearing the relevant portions of the crystals using MD simulations is found to normally relax to lower energies than the other methods. In particular, as will be described below, an MD scheme illustrated in Figure 3 is effective in

Table 1. Dislocation Line Energies in CdTe Crystals

seven glide partial dislocations				
$\vec{\xi}$	$\vec{b}$	θ (°)	type	energy (eV/Å)
$[11\bar{2}]$	$[11\bar{2}]/6$	0	α (=β)	0.38
$[11\bar{2}]$	$[\bar{2}11]/6$	120	α	0.63
$[11\bar{2}]$	$[\bar{2}11]/6$	120	β	0.63
$[1\bar{1}0]$	$[11\bar{2}]/6$	90	α	0.70
$[1\bar{1}0]$	$[11\bar{2}]/6$	90	β	0.70
$[1\bar{1}0]$	$[1\bar{2}1]/6$	330	α	0.44
$[1\bar{1}0]$	$[1\bar{2}1]/6$	330	β	0.45

11 glide perfect dislocations (dissociated)					
$\vec{\xi}$	$\vec{b}$	θ (°)	Shockley dissociations	type	energy (eV/Å)
$[1\bar{1}0]$	$[1\bar{1}0]/2$	0	$[1\bar{2}1]/6$ $[2\bar{1}\bar{1}]/6$	α (=β)	0.69
$[1\bar{1}0]$	$[10\bar{1}]/2$	60	$[11\bar{2}]/6$ $[2\bar{1}\bar{1}]/6$	α	1.38
$[1\bar{1}0]$	$[10\bar{1}]/2$	60	$[11\bar{2}]/6$ $[2\bar{1}\bar{1}]/6$	β	1.38
$[1\bar{1}0]$	$[10\bar{1}]/2$	300	$[1\bar{2}1]/6$ $[\bar{1}\bar{1}2]/6$	α	1.38
$[1\bar{1}0]$	$[0\bar{1}1]/2$	300	$[1\bar{2}1]/6$ $[\bar{1}\bar{1}2]/6$	β	1.38
$[11\bar{2}]$	$[01\bar{1}]/2$	30	$[11\bar{2}]/6$ $[\bar{1}2\bar{1}]/6$	α	1.05
$[11\bar{2}]$	$[01\bar{1}]/2$	30	$[11\bar{2}]/6$ $[\bar{1}2\bar{1}]/6$	β	1.03
$[11\bar{2}]$	$[\bar{1}10]/2$	90	$[\bar{2}11]/6$ $[\bar{1}2\bar{1}]/6$	α	1.60
$[11\bar{2}]$	$[\bar{1}10]/2$	90	$[\bar{2}11]/6$ $[\bar{1}2\bar{1}]/6$	β	1.55
$[11\bar{2}]$	$[\bar{1}01]/2$	150	$[\bar{2}11]/6$ $[\bar{1}\bar{1}2]/6$	α	1.04
$[11\bar{2}]$	$[\bar{1}01]/2$	150	$[\bar{2}11]/6$ $[\bar{1}\bar{1}2]/6$	β	1.03

11 glide perfect dislocations (undissociated)				
$\vec{\xi}$	$\vec{b}$	θ (°)	type	energy (eV/Å)
$[1\bar{1}0]$	$[1\bar{1}0]/2$	0	α (=β)	0.79
$[1\bar{1}0]$	$[10\bar{1}]/2$	60	α	1.51
$[1\bar{1}0]$	$[10\bar{1}]/2$	60	β	1.66
$[1\bar{1}0]$	$[10\bar{1}]/2$	300	α	1.56
$[1\bar{1}0]$	$[0\bar{1}1]/2$	300	β	1.53
$[11\bar{2}]$	$[01\bar{1}]/2$	30	α	1.32
$[11\bar{2}]$	$[01\bar{1}]/2$	30	β	1.16
$[11\bar{2}]$	$[\bar{1}10]/2$	90	α	1.73
$[11\bar{2}]$	$[\bar{1}10]/2$	90	β	1.77
$[11\bar{2}]$	$[\bar{1}01]/2$	150	α	1.14
$[11\bar{2}]$	$[\bar{1}01]/2$	150	β	1.15

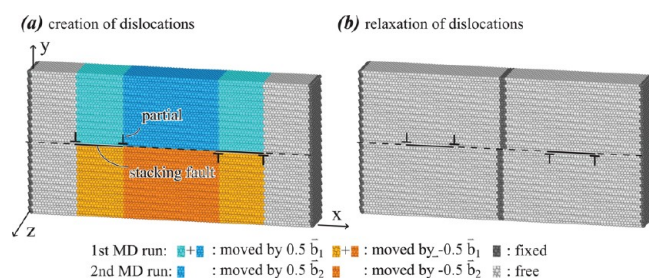| 11 shuffle dislocations				
$\vec{\xi}$	$\vec{b}$	θ (°)	type	energy (eV/Å)
$[1\bar{1}0]$	$[1\bar{1}0]/2$	0	α (=β)	0.81
$[1\bar{1}0]$	$[10\bar{1}]/2$	60	α	1.46
$[1\bar{1}0]$	$[10\bar{1}]/2$	60	β	1.46
$[1\bar{1}0]$	$[0\bar{1}1]/2$	300	α	1.49
$[1\bar{1}0]$	$[0\bar{1}1]/2$	300	β	1.49
$[11\bar{2}]$	$[01\bar{1}]/2$	30	α	1.05
$[11\bar{2}]$	$[01\bar{1}]/2$	30	β	1.05
$[11\bar{2}]$	$[\bar{1}10]/2$	90	α	1.70
$[11\bar{2}]$	$[\bar{1}10]/2$	90	β	1.70
$[11\bar{2}]$	$[\bar{1}01]/2$	150	α	1.07
$[11\bar{2}]$	$[\bar{1}01]/2$	150	β	1.07

creating partial, undissociated perfect, and shuffle dislocations, and an MD scheme illustrated in Figure 4 is effective in creating dissociated perfect dislocations. These schemes enable atom positions to be strictly determined from atom interactions and also best reflects realistic scenario that dislocations are created under local shear stresses.

The computational system used is periodic in the x and z axes with free surfaces along the y axis. For the undissociated
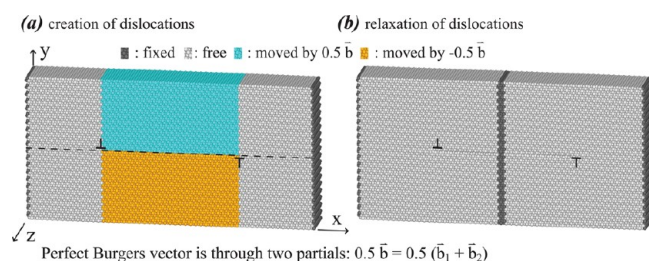
Figure 3. Line energy model for partial, undissociated perfect, and shuffle dislocations. (a) MD simulations to create dislocations and (b) MD and MS simulations to relax dislocations.


Figure 4. Line energy model for dissociated perfect dislocations. (a) MD simulations to create dislocations and (b) MD and MS simulations to relax dislocations.

dislocations (including partial and shuffle dislocations) shown in Figure 3, the system is divided into different regions as

indicated by blue (middle upper), orange (middle lower), black (left and right), and white (the rest) colors. With the black regions held fixed and the white regions free to relax, an MD simulation is first performed to uniformly move the blue region by half of the Burgers vector $0.5\vec{b}$ and the orange region by negative half of the Burgers vector $-0.5\vec{b}$. For partial dislocations, the movement of the blue and orange regions is completed directly over a total simulated time of 0.1 ns. For perfect dislocations, the movement is through two stages over a total simulated time of 0.2 ns to follow the lowest energy path of two partials, i.e., $0.5(\vec{b}_1 + \vec{b}_2)$ $(=0.5\vec{b})$ for the blue region and $-0.5(\vec{b}_1 + \vec{b}_2)$ $(=-0.5\vec{b})$ for the orange region. In addition, the system temperature is uniformly decreased from 300 to 10 K during simulation. This MD procedure creates two dislocations with opposite Burgers vectors (also note that if the dislocations have an edge component, then one is an α and the other one is a β dislocation) as shown in Figure 3a.

For the dissociated perfect dislocations shown in Figure 4, the system is divided into different regions as indicated by light and dark blue (middle upper), light and dark orange (middle lower), black (left and right), and white (the rest) colors. With the black regions held fixed and the white regions free to relax, an MD simulation is first performed to uniformly move the light and dark blue region by half of a Shockley partial Burgers vector $0.5\vec{b}_1$ and the light and dark orange region by negative half of the same Shockley partial Burgers vector $-0.5\vec{b}_1$ over a total simulated time of 0.1 ns. A second MD simulation is then performed to move the dark blue region by half of the other
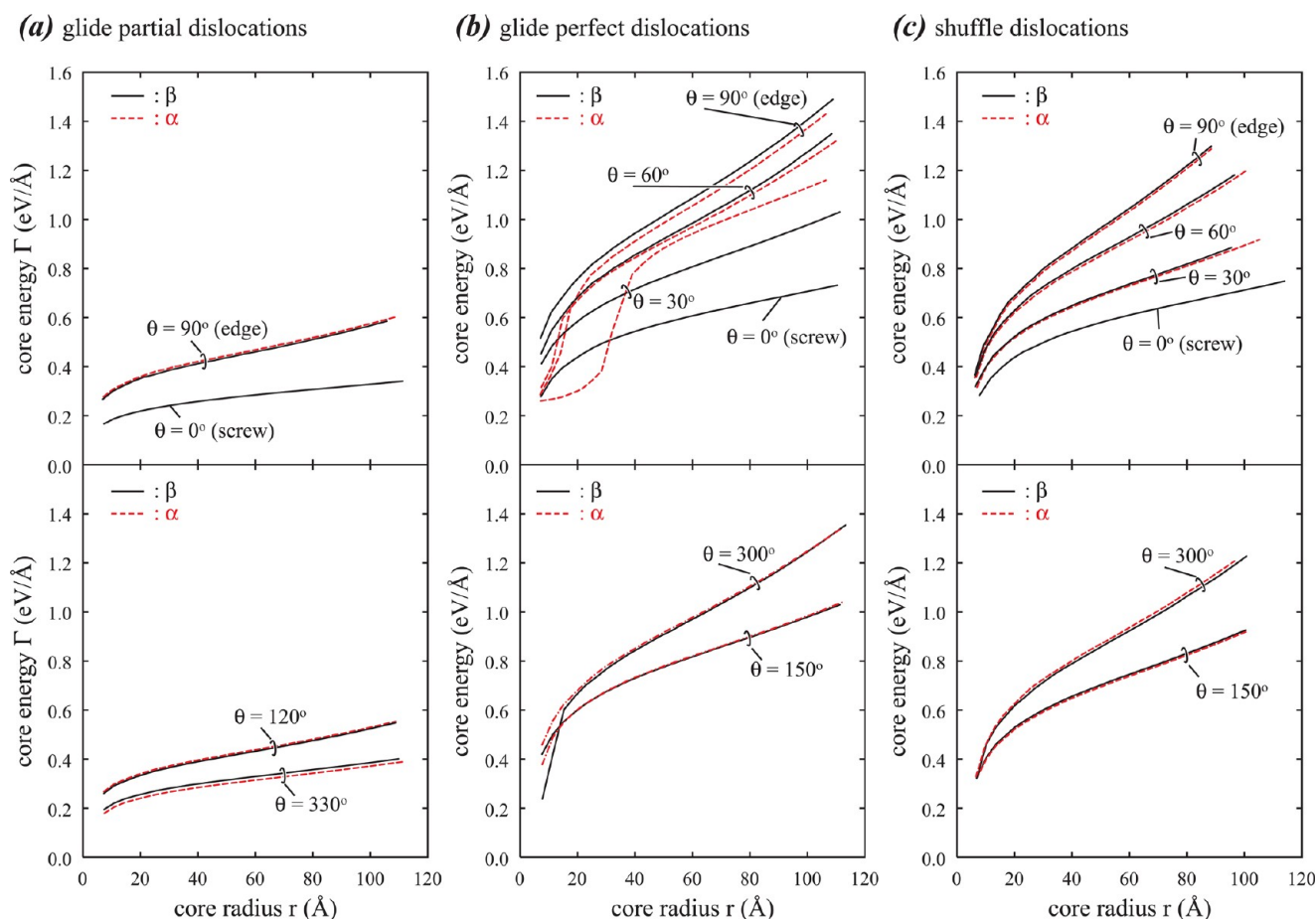
Figure 5. Dislocation line energy as a function of core radius. (a) Glide partial dislocations, (b) glide perfect dislocations, and (c) shuffle dislocations.
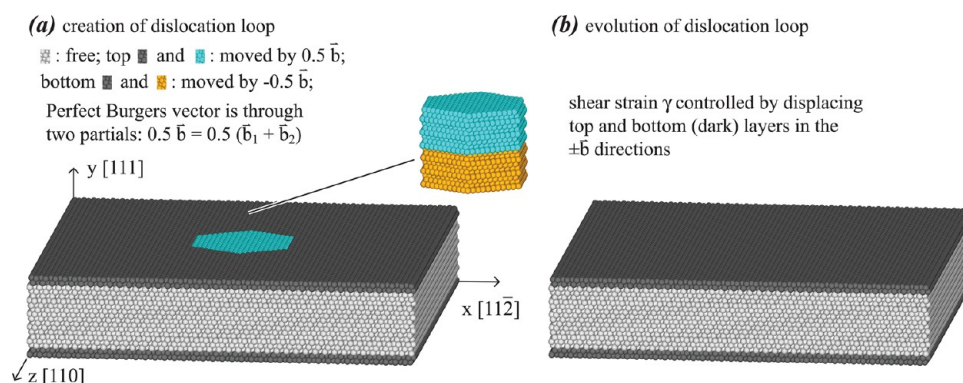
Figure 6. Dislocation loop model. (a) MD simulation to create dislocation loop and (b) MD simulation to evolve dislocation loop.

Shockley partial Burgers vector $0.5\vec{b}_2$ and the dark orange region by negative half of the same Shockley partial Burgers vector $-0.5\vec{b}_2$ over another total simulated time of 0.1 ns. In addition, the system temperature is uniformly decreased from 300 to 10 K during these two simulations. This MD procedure creates the same two perfect dislocation Burgers vectors as shown in Figure 3a except that each perfect dislocation is dissociated into two Shockley partials bounding a stacking fault band as shown in Figure 4a.

Once dislocations are created in the MD simulations, the blue and orange regions are released. A narrow region in the middle of the system is allocated as shown by the black color in Figures 3b and 4b. For perfect dislocations, this narrow region remains a perfect crystal because the blue region is moved by a perfect Burgers vector with respect to the orange region. For partial dislocations, the narrow middle region contains a stacking fault. With left, right, and middle black regions fixed, an MS simulation is then conducted to relax the dislocations.

In this work, we use an edge dislocation geometry containing 97 $(\bar{1}10)$ planes in the x direction, 60 (111) planes in the y direction, and 24 $(11\bar{2})$ planes in the z direction and a screw dislocation geometry containing 168 $(11\bar{2})$ planes in the x direction, 60 (111) planes in the y direction, and 14 $(1\bar{1}0)$ planes in the z direction to create various perfect and dislocated computational crystals. Relaxed energies of both dislocated and perfect crystals are calculated. To separate α and β dislocation effects, the total energy is split to the left and right parts respectively by summing up the atomic energies of the left and right halves of the systems. The line energies of the left and the right dislocation, Γ_i, are then calculated as $\Gamma_i = (E_{d,i} - E_{0,i} - w_i L_z \gamma_{sf})/L_z$, where E_d and E_0 are the relaxed energies of the dislocated and the perfect crystals, respectively, L_z is the dislocation length (= system dimension in the z axis), γ_{sf} is the stacking fault energy, w is the stacking fault bandwidth, and the subscript i (= l or r) indicates the left and the right dislocations. The results obtained are summarized in Table 1.

The relaxed configurations obtained from the energy minimization simulations were visualized. We find that of all the simulations using the initial perfect dislocations, the maximum splitting distance is only 25 Å after energy minimization. This confirms that these dislocations indeed remain approximately undissociated. Table 1 indicates that the screw ($\theta = 0°$) dislocations have lower energies than other dislocations, being 0.38, 0.69, 0.79, and 0.81 eV/Å for partial, dissociated perfect, undissociated perfect, and shuffle dislocations, respectively. Interestingly, the acute angle of the second lowest energy (shuffle, glide partial, glide perfect) dislocations

all equal 30° (e.g., $\theta = 30°$, 150°, and 330°). In addition, the energies of dissociated perfect dislocations are about 80−92% of the energies of undissociated dislocations, suggesting that the dissociated dislocations are more stable. However, the observation that the perfect dislocations remain approximately undissociated during MD and energy minimization simulations suggests an energy barrier of dissociation. The configuration of perfect dislocations will be examined further below in MD simulations of dislocation motion.

The dislocation line energy is not a constant material property, but rather increases with the material volume within a radius r from the dislocation core. The dislocation line energy at a given radius r can be calculated using the same approach described above except that the energies of the perfect and dislocated crystals are taken as the sum of the atomic energies for all the atoms within the radius. The dislocation line energies as a function of r thus obtained are shown in Figure 5a−c for partial, (undissociated) perfect, and shuffle dislocations respectively.

Figure 5a−c indicates that dislocation line energies calculated with the atomistic models linearly increase with dislocation radius r when r is larger than 40 Å. This is consistent with the boundary conditions used in Figures 3 and 4 where the black regions are held fixed during simulations. The dislocation core energies at small radii, say $r < 30$ Å, come from the relaxed dislocation core structures. In the present work, the system sizes have been chosen to be sufficiently large so that the predicted dislocation core structures are independent of the boundary conditions. As a result, our simulations can give accurate dislocation core energies at $r < 30$ Å that cannot be predicted from linear elastic theories. It can be seen from Figure 5a−c that dislocation energies sharply decrease when the radius is decreased. In addition, α and β dislocations have similar energy vs r curves for partial and shuffle dislocations. While α and β dislocation energies are also similar for the perfect dislocations at large radii, they become different at the core. In particular, the α perfect dislocation core energies are lower than the β perfect dislocation core energies.
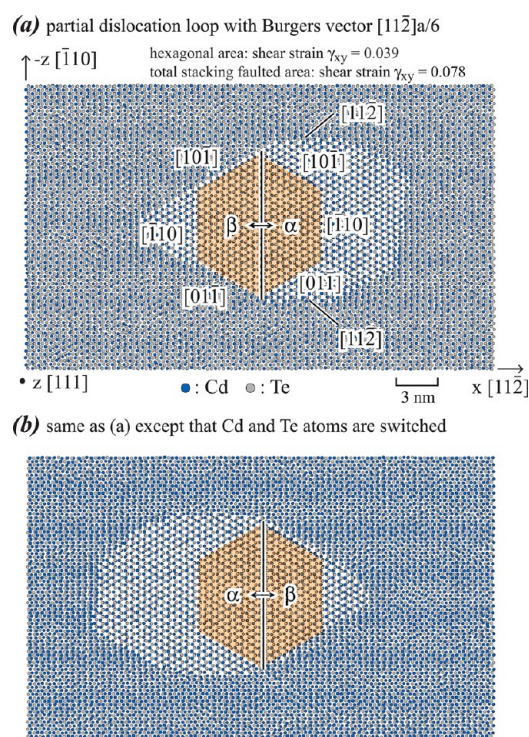
VI. DISLOCATION LOOP EVOLUTION UNDER SHEAR

One effective approach to simultaneously study the motion of multiple dislocations is to examine the evolution of a dislocation loop under a shear stress. The computational system consists of a CdTe crystal with 120 $(11\bar{2})$ planes in the x direction, 18 (111) planes in the y direction, and 68 $(1\bar{1}0)$ planes in the z direction. Periodic boundary conditions are used in the x and z directions and a free boundary condition is used

in y direction during the simulation. To create a dislocation loop, the system is divided into different regions as shown in Figure 6(a): the black (top and bottom) regions, the blue (middle upper) hexagonal region, the orange (middle lower) hexagonal region, and the white (remaining) region. As plastic deformation usually proceeds through a glide of dislocations, we focus on glide dislocations. Hence, we assume that the boundary between the upper and lower hexagons is between planes A and B as defined in Figures 1a and 2a. To create a realistic dislocation loop with a Burgers vector of $\vec{b}$, an MD simulation is performed to uniformly move the top black and blue regions by $0.5\vec{b}$ and the lower black and orange regions by $-0.5\vec{b}$ over a simulated time of 0.1 ns while allowing the white region to relax according to Newton's equation of motion and a constant temperature of 10 K. As mentioned above, for a partial dislocation loop, the MD simulation is completed directly, and for a perfect dislocation loop, the MD simulation is completed in two stages to follow the low energy path of two partial dislocations. This MD simulation procedure creates a dislocation loop at a shear strain of approximately $\gamma = b/t$, where b is the magnitude of the dislocation Burgers vector and t is the thickness of the sample. The system is then redivided into three regions as shown in Figure 6b: the black (top and bottom) regions and the white (remaining) region. The evolution of dislocation loops is examined in subsequent MD simulations at a high temperature of 900 K where the top and bottom surface black layers are further moved in positive and negative Burgers vector directions to increase the shear strain.

A. Partial Dislocation Loop. A partial dislocation Burgers vector of $[11\bar{2}]a/6$ is used to create an initial dislocation loop using the procedure shown in Figure 6(a). This procedure produces a shear strain of $\gamma_{xy} = 0.039$. Further shear strain is applied by moving the top and bottom black regions in the $+x$ and $-x$ directions by 1.394 Å, respectively, using the procedure shown in Figure 6b. This corresponds to a total shear strain of $\gamma_{xy} = 0.078$. The equilibrium dislocation loop configurations obtained at 900 K temperature are examined in Figure 7 by showing the top view of four consecutive planes above and below the slip plane, where blue and gray circles indicate Cd and Te atoms respectively, and the yellow hexagon indicates the initial partial dislocation loop at $\gamma_{xy} = 0.039$. Panels a and b in Figure 7 are obtained using exactly the same conditions except that the Cd and Te atoms are switched between the two figures, so that in Figure 7a, the right side of the loop is an α dislocation and the left side of the loop is a β dislocation, whereas in Figure 7b, the left side is α and the right side is β.

Because the movement of a partial dislocation leaves behind a stacking fault, the relaxed partial dislocation loop can be identified by the boundary of the two stacking patterns demonstrated in the figure. It can be seen from Figure 7a that the hexagonal dislocation loop becomes asymmetric under the shear and in particular, the α dislocation moves by a far longer distance than the β dislocation. This is further verified in Figure 7b where the asymmetry of the dislocation is flipped as a consequence of the flip of α and β dislocations. This simulation strongly indicates that α dislocations are much more mobile than β dislocations (despite their similar line energies in Table 1), in good agreement with experiments conducted for many semiconductor compounds.[22,23]

One interesting observation in Figure 7 is that to accommodate the motion of the α segment ($\vec{\xi} = [\bar{1}10]$) of the dislocation loop, two segments ($\vec{\xi} = [11\bar{2}]$) are created. These segments are perpendicular to the α segment and are

(a) partial dislocation loop with Burgers vector $[11\bar{2}]a/6$

(b) same as (a) except that Cd and Te atoms are switched

Figure 7. Evolution of a $[11\bar{2}]a/6$ partial dislocation loop. (a) Configurations at strains $\gamma_{xy} = 0.039$ and $\gamma_{xy} = 0.078$ and (b) the same as in panel a except that Cd and Te atoms are switched.

screw partials. This means that the motion of the mobile α partial dislocations can cause elongated screw partials. As a result, CdTe crystals may have a high density of such type of screw partials, in agreement with its low energy shown in Table 1. On the other hand, the β type of edge partial dislocations disappear upon the strain. This corresponds well to the high energy of the edge partial in Table 1.

B. Perfect Dislocation Loop. A perfect dislocation loop with a Burgers vector of $[\bar{1}10]a/2$ is created using the procedure described in Figure 6a. This procedure produces an initial shear strain of $\gamma_{yz,0} = 0.068$. By moving the top and bottom black regions in the $+z$ and $-z$ directions at a constant speed of 1.2 nm/ns during an MD simulation at 900 K, as described in Figure 6b, the system is further deformed at a strain rate of $d\gamma_{yz}/dt = 0.338$/ns. The configuration of the dislocation loop during the further strain is shown in Figures 8a−d as a function of time, where the color scheme represents the magnitude of the slip vector developed previously to show dislocations.[24] Figure 8a shows that shortly after further strain at $t = 0.0025$ ns ($\gamma_{yz} = 0.069$), the dislocation loop remains hexagonal but some portion of the α dislocation (the lower part of the $[10\bar{1}]$ section) bows out. Figure 8b shows that at $t = 0.0100$ ns ($\gamma_{yz} = 0.071$), the dislocation bows out more. In Figure 8c at 0.0250 ns ($\gamma_{yz} = 0.076$), the α dislocation is seen to have moved a significant distance that causes it to pass through the low boundary and enter into the image from the top boundary under the periodic boundary condition. In contrast, little movement is seen for the β dislocation. Clearly, perfect α dislocations are also much more mobile than perfect β dislocations (despite their similar line energies shown in Table 1), in good agreement with experiments.[22] Interestingly, Figure 8c indicates that, although screw dislocations also have
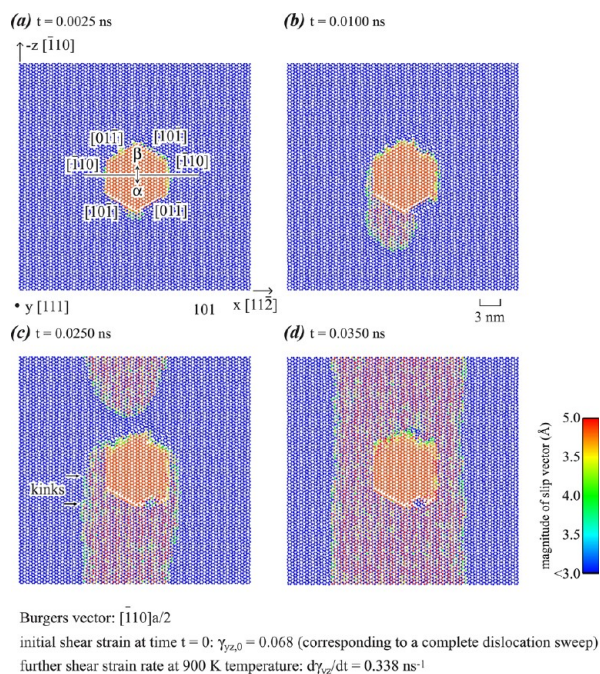
Figure 8. Evolution of a $[\bar{1}10]/2$ perfect dislocation loop. $t = 0.0025$ (a), 0.0100 (b), 0.0250 (c), and 0.0350 ns (d).

higher mobility than β edge dislocations, they are much less mobile than α edge dislocations.

When the α dislocation meets the β dislocation at the top of the hexagon, they are annihilated, and the dislocation loop becomes two vertical screw dislocations running across the periodic dimension in the z direction, as can be seen in Figure 8d at $t = 0.035$ ns ($\gamma_{yz} = 0.080$). Further strain will cause the two dislocations to continuously move in the $\pm x$ directions until they completely sweep the entire area and are annihilated. Interestingly, we find that the dislocation motion is thermally activated and does not occur when the simulation is performed at a low temperature, say, 10 K. In addition, we find that the dislocations do not move as straight lines, but rather through the formation and rapid motion of kinks along the z direction as shown in Figure 8c. This is consistent with the traditional kink model of thermally activated motion of dislocations.[25]

The observation that screw dislocations are much less mobile than α edge dislocations indicates that when the α sector of a dislocation loop moves, the screw dislocation sectors ($\vec{\xi} = [\bar{1}10]$) will elongate. As a result, screw dislocations can have a

high density in the crystal. This is consistent with the low energies of screw dislocations shown in Table 1. In addition, no dislocation dissociation is observed in Figure 8, indicating that the perfect dislocations do not necessarily dissociate under nonequilibrium conditions. This is consistent with the discussions presented above.
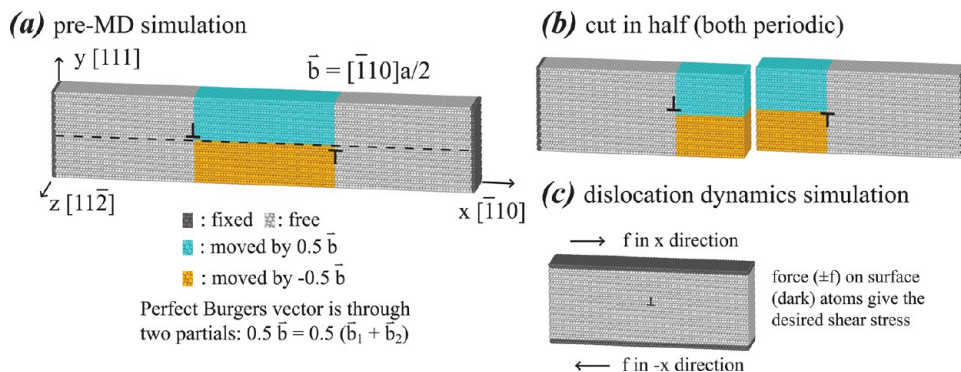
VII. DISLOCATION MOBILITIES

The details of dislocation mobility are important to understand because they directly control dislocation network structures. For thermally activated motion of dislocations, the dislocation velocity can be expressed as[26]

$$v = v_0 \exp\left(-\frac{Q - \tau\Omega}{kT}\right) \tag{1}$$

where Q and Ω are respectively the activation energy and activation volume of the dislocation motion, τ is the shear stress, k is Boltzmann's constant, T is the temperature, and v_0 is a constant representing saturation dislocation velocity for barrierless (very high temperature or shear stress) dislocation motion. Here Q and Ω are the primary parameters quantifying dislocation mobility.

The discussion presented above already indicates several distinctive dislocation types that may determine dislocation structures. First, α and β partial and perfect dislocations have a strong edge component and can contribute to the climb motion responsible for the formation of small angle grain boundaries. α dislocations are the most mobile, resulting in special structural features of dislocation networks. Screw partial and perfect dislocations can also be important. These screw dislocations are expected to have a high density as they have low energies and can be created by the motion of α dislocations. The objective of the present work is not to exhaustively tabulate the mobilities of a variety of dislocations. Hence, we focus on calculating the activation energy barrier Q and activation volume Ω for α and β edge type of perfect dislocations. Such studies will allow us to fully explore the method for calculating Q and Ω and to validate the results using known experimental relative mobilities of α and β dislocations. In addition, edge dislocations play an important role in dislocation network formation due to their climb motion. The extension of the method to other dislocations that can provide complete inputs for simulations of dislocation network structure evolution using larger scale (e.g., dislocation dynamics[27]) models will be performed in future work.


Figure 9. Edge dislocation mobility model. (a) MD simulation to create α and β dislocations, (b) isolate out α and β dislocations, and (c) MD simulation to evolve dislocation under shear stress τ_{xy}.

The activation energy barriers of dislocation motion are often directly calculated from energy profiles using the nudged elastic band method.[28−31] However, the stop-action observation of the dislocation migration case shown in Figure 8 indicates that the thermally activated motion of dislocations proceeds through a variety of different paths. Without requiring an explicit treatment of migration paths, we perform MD simulations of dislocation motion at a variety of temperatures and shear stresses to fit an apparent activation energy barrier and activation volume directly from (1). The activation energy determined this way pertains to a free energy barrier that incorporates the multiple path (entropy) effects. In addition, this approach provides a direct verification of (1) and, hence, the thermally activated dislocation mechanism.

The model for performing dislocation motion simulations is shown in Figure 9. The initial crystal contains 144 ($\overline{1}$10) planes in the x direction, 36 (111) planes in the y direction, and 24 (11$\overline{2}$) planes in the z direction. The system employs periodic boundary conditions in x and z directions and a free boundary condition in y direction. First, the initial crystal is divided into different regions as shown in Figure 9a: the black (left and right) regions, the blue (middle upper) region, the orange (middle lower) region, and the white (remaining) region. Since we only explore glide dislocations, we assume that the boundary between the blue and orange regions is between A and B planes as defined in Figures 1a and 2a. To create dislocations with a perfect Burgers vector of $\vec{b} = \vec{b}_1 + \vec{b}_2$, an MD simulation is performed where the black regions are fixed, the white regions are relaxed, and the blue and orange regions are first uniformly moved by $0.5\vec{b}_1$ and $-0.5\vec{b}_1$, respectively, over a simulated time of 0.001 ns and then moved by $0.5\vec{b}_2$ and $-0.5\vec{b}_2$, respectively, over another simulated time of 0.001 ns. The crystal is then cut in half in the x direction as shown in Figure 9b with a corresponding adjustment of the periodic length so that the two halves remain periodic in the x direction. This procedure essentially creates two crystals, each containing one perfect dislocation. In particular, we use $\vec{b} = [\overline{1}10]a/2$, $\vec{b}_1 = [\overline{1}2\overline{1}]a/6$, and $\vec{b}_2 = [\overline{2}11]a/6$ to create two crystals, one containing an α perfect dislocation, and the other one containing a β perfect dislocation.

For dislocation motion simulations, the (half) system is divided into three regions: the black (top and bottom) regions and the white (remaining) region. By adding corresponding forces to the atoms in the top and bottom regions in $+x$ and $-x$ directions, respectively, a desired shear stress τ_{xy} can be applied. Molecular dynamics simulations under an NPT (constant atom number, pressure, and temperature) condition are then performed to study migration of dislocations at a variety of stresses and temperatures. We find that in all of these simulations the dislocation splitting is very small, further verifying the discussions presented above that perfect dislocations do not necessarily dissociate. Assuming that the slip vector[24] reaches a maximum at the dislocation core, the dislocation position is calculated as a function of time. Results obtained for α and β dislocations at selected stresses and temperatures are shown in Figure 10. It can be seen from Figure 10 that all the dislocation vs time curves approximately fall on straight lines. This shows that the data can provide reliable information about the steady-state dislocation velocity. The slope of these straight lines changes with stress and temperature, indicating that the simulated conditions capture the thermally activated mechanisms of dislocation motion.
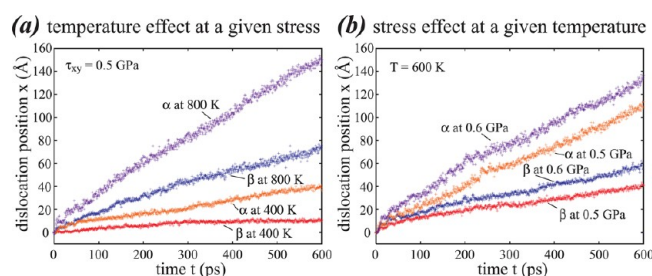
Figure 10. Dislocation position as a function of time. (a) Effect of temperature at a given stress and (b) effect of stress at a given temperature.

Figure 10a shows the effect of temperature on dislocation motion at a constant shear stress of 0.5 GPa. Increasing the temperature is seen to increase the dynamics, consistent with the thermal activation mechanism. At the same temperature, the α dislocation is seen to move faster than the β dislocation, further verifying the results seen in Figures 7 and 8. Figure 10b shows the effect of shear stress at a constant temperature of 600 K. Here increasing the stress also correctly increases the dislocation velocity, and the α dislocation is again validated to move faster than the β dislocation.

The steady state velocity can be easily calculated from the slope of the curves shown in Figure 10. The results obtained at a constant shear stress of $\tau_{xy} = 0.5$ GPa are plotted as $\ln(v)$ vs $(kT)^{-1}$ curves in Figure 11. Here the unfilled and filled circles
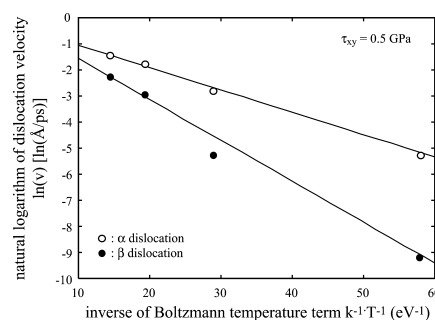
Figure 11. Arrhenius relation between dislocation velocity and temperature.

represent MD data for α and β dislocations respectively, and the lines are fitted to the data using Equation (1). Figure 11 indicates that the MD data falls fairly well on straight $\ln(v)$ vs $(kT)^{-1}$ lines, validating that the method indeed captures well the thermally activated dislocation migration. Through the fitting, we find that the activation energy and activation volume are $Q = 0.14$ eV and $\Omega = 17$ Å^3 for the α dislocation and $Q = 0.27$ eV and $\Omega = 38$ Å^3 for the β dislocation. This again verifies that in the thermally activated regime (e.g., $\tau_{xy} \ll 1$ GPa), the α dislocation is more mobile than the β dislocation.

The thermally activated plastic deformation of CdTe has been experimentally analyzed below room temperature.[32] The activation energy and activation volume are assumed to decrease with increasing stress in the experiments. Under this assumption, the fitted experimental activation energy and activation volume are approximately 0.8 eV and 5500 Å^3, respectively, at a small stress of 0.005 GPa, and fall to <0.5 eV and <2250 Å^3, respectively, at a stress of 0.010 GPa. Here we assume that Q and Ω are constant and are fitted using MD data at high stresses (e.g., 0.5 GPa). In addition, simulations target

only the Peierls potential barrier mechanism of specific (α and β perfect edge) dislocations, whereas, experiments may include point defect obstacle mechanisms and the contributions from other dislocations.[32] As a result, it is expected that the simulated activation energy and activation volume are smaller than their experimental counterparts.

VIII. CONCLUSION

Our BOP-based MD simulations of dislocations in CdTe crystals lead to the following conclusions:

(1) α dislocations move much faster than β dislocations, in good agreement with well-known experiments for semiconductor compounds. This, along with previous demonstrations that our BOP captures properties of many phases and predicts crystalline growth during MD simulations of chemical vapor deposition[17,19] and melt-growth,[18] provides strong validation that the BOP correctly captures the physics of dislocation motion in CdTe. The BOP-based MD simulations, therefore, can provide high-fidelity data to construct large scale (e.g., dislocation dynamics[27]) models that can simulate the evolution of dislocation cell structures.

(2) For partial, perfect, and shuffle sets, screw dislocations always have the lowest energies. Dissociated glide dislocations always have lower energies than perfect glide dislocations. However, perfect glide dislocations do not necessarily dissociate due to the energy barrier of dissociation. In particular, the splitting distance of perfect glide dislocations is seen to remain very small in our dynamic MD simulations.

(3) The acute angle of the second lowest energy (shuffle, glide partial, glide perfect) dislocations all equal 30° (e.g., θ = 30°, 150°, 330°).

(4) Screw dislocations are much less mobile than α edge dislocations. As a result, the screw dislocation sectors perpendicular to the α sector are elongated when an α sector of a dislocation loop moves. This suggests that screw dislocations are likely to have a higher density than edge dislocations, in good agreement with the low screw dislocation energies.

(5) Without calculating the energy profile explicitly, we show that MD simulations of dislocation motion at a variety of stresses and temperatures can be used to effectively deduce the activation free energy barrier and activation volume of thermally activated glide of dislocations. In particular, we found activation free energy barriers of 0.14 and 0.27 eV and activation volumes of 17 and 36 Å^3, respectively, for α and β edge types of glide dislocations.

■ AUTHOR INFORMATION

Corresponding Author
*E-mail: xzhou@sandia.gov.
Notes
The authors declare no competing financial interest.

■ ACKNOWLEDGMENTS

■ REFERENCES

(1) Schlesinger, T. E.; Toney, J. E.; Yoon, H.; Lee, E. Y.; Brunett, B. A.; Franks, L.; James, R. B. *Mater. Sci. Eng.* **2011**, *32*, 103−189.
(2) Sellin, P. J. *Nucl. Instrum. Methods Phys. Res., Sect. A* **2003**, *513*, 332−339.
(3) Peurrung, A. *Mater. Today* **2008**, *11*, 50−54.
(4) Takahashi, T.; Watanabe, S. *IEEE Trans. Nucl. Sci.* **2001**, *48*, 950−959.
(5) Bolotnikov, A. E.; Camarda, G. S.; Carini, G. A.; Cui, Y.; Li, L.; James, R. B. *Nucl. Instrum. Methods Phys. Res., Sect. A* **2007**, *579*, 125−129.
(6) Bolotnikov, A. E.; Camarda, G. S.; Carini, G. A.; Cui, Y.; Li, L.; James, R. B. *Nucl. Instrum. Methods Phys. Res., Sect. A* **2007**, *571*, 687−698.
(7) Szeles, C. *Phys. Status Solidi A* **2004**, *241*, 783−790.
(8) Szeles, C. *IEEE Trans. Nucl. Sci.* **2004**, *51*, 1242−1249.
(9) Zha, G. Q.; Jie, W. Q.; Tan, T. T.; Wang, L. H. *Phys. Status Solidi A* **2007**, *204*, 2196−2200.
(10) Babentsov, V.; Boiko, V.; Schepelskii, G. A.; James, R. B.; Franc, J.; Prochazka, J.; Hlidek, P. *Nucl. Instrum. Methods Phys. Res., Sect. A* **2011**, *633*, S81−S82.
(11) Zeng, D. M.; Jie, W. Q.; Wang, T.; Zha, G. Q.; Zhang, J. J. *Nucl. Instrum. Methods Phys. Res., Sect. A* **2008**, *586*, 439−443.
(12) Ward, D. K.; Zhou, X. W.; Wong, B. M.; Doty, F. P.; Zimmerman, J. A. *Phys. Rev. B* **2012**, *85*, 115206−19.
(13) Ward, D. K.; Zhou, X. W.; Wong, B. M.; Doty, F. P.; Zimmerman, J. A. *J. Chem. Phys.* **2011**, *134*, 244703−13.
(14) Ward, D. K.; Zhou, X. W.; Wong, B. M.; Doty, F. P.; Zimmerman, J. A. submitted.
(15) LAMMPS download site: lammps.sandia.gov.
(16) Plimpton, S. *J. Comput. Phys.* **1995**, *117*, 1−19.
(17) Zhou, X. W.; Ward, D. K.; Wong, B. M.; Doty, F. P.; Zimmerman, J. A.; Nielson, G. N.; Cruz-Campa, J. L.; Gupta, V. P.; Granata, J. E.; Chavez, J. J.; Zubia, D. *Phys. Rev. B* **2012**, *85*, 245302−15.
(18) Zhou, X. W.; Ward, D. K.; Wong, B. M.; Doty, F. P. *Phys. Rev. Lett.* **2012**, *108*, 245503−4.
(19) Chavez, J. J.; Ward, D. K.; Wong, B. M.; Doty, F. P.; Cruz-Campa, J. L.; Nielson, G. N.; Gupta, V. P.; Zubia, D.; McClure, J.; Zhou, X. W. *Phys. Rev. B* **2012**, *85*, 245316−4.
(20) Vere, A. W.; Cole, S.; Williams, D. J. *J. Electron. Mater.* **1983**, *12*, 551−561.
(21) Winkler, M.; Schenk, M.; Hahnert, I. *Cryst. Res. Technol.* **1992**, *27*, 1047−1051.
(22) Vanderschaeve, G.; Levade, C.; Caillard, D. *J. Phys.: Condens. Matter* **2000**, *12*, 10093−10103.
(23) Ninomiya, T. *J. Phys. (Paris)* **1979**, *40*, 143−145.
(24) Zhou, X. W.; Doty, F. P.; Yang, P. *J. Appl. Phys.* **2010**, *107*, 123509−11.
(25) Hirth, J. P.; Lothe, J. *Theory of Dislocations*; Wiley: Hoboken, NY, 1982.
(26) Hull, D.; Bacon, D. J. *Introduction to Dislocations*; Butterworth-Heinemann: Oxford, U.K., 2001; p 195.
(27) Bulatov, V. V.; Cai, W. *Computer Simulation of Dislocations*; Oxford University Press: Oxford, U.K., 2006.
(28) Henkelman, G.; Jonsson, H. *J. Chem. Phys.* **2000**, *113*, 9978−9985.
(29) Henkelman, G.; Uberuaga, B. P.; Jonsson, H. *J. Chem. Phys.* **2000**, *113*, 9901−9904.
(30) Zhu, T.; Li, J.; Samanta, A. ; Kim, H. G.; Suresh, S. *Proc. Natl. Acad. Sci. U.S.A.* **2007**, *104*, 3031−3036.
(31) Shima, K.; Izumi, S.; Sakai, S. *J. Appl. Phys.* **2010**, *108*, 063504−3.
(32) Maeda, K.; Nakagawa, K.; Takeuchi, S. *Phys. Status Solidi A* **1978**, *48*, 587−591.